J. Fluid Mech. (1998), *vol.* 358, *pp.* 1–28. Printed in the United Kingdom

© 1998 Cambridge University Press

Motion of an array of drops through a cylindrical tube

By C. COULLIETTE AND C. POZRIKIDIS

Department of Applied Mechanics and Engineering Sciences, University of California, San Diego, La Jolla, CA 92093-0411, USA

(Received 4 December 1996 and in revised form 7 October 1997)

We study the pressure-driven transient motion of a periodic file of deformable liquid drops through a cylindrical tube with circular cross-section, at vanishing Reynolds number. The investigations are based on numerical solutions of the equations of Stokes flow obtained by the boundary-integral method. It is assumed that the viscosity and density of the drops are equal to those of the suspending fluid, and the interfaces have constant tension. The mathematical formulation uses the periodic Green's function of the equations of Stokes flow in a domain that is bounded externally by a cylindrical tube, which is computed by tabulation and interpolation. The surface of each drop is discretized into quadratic triangular elements that form an unstructured interfacial grid, and the tangential velocity of the grid-points is adjusted so that the mesh remains regular for an extended but limited period of time. The results illustrate the nature of drop motion and deformation, and thereby extend previous studies for axisymmetric flow and small-drop small-deformation theories. It is found that when the capillary number is sufficiently small, the drops start deforming from a spherical shape, and then reach slowly evolving quasi-steady shapes. In all cases, the drops migrate radially toward the centreline after an initial period of rapid deformation. The apparent viscosity of the periodic suspension is expressed in terms of the effective pressure gradient necessary to drive the flow at constant flow rate. For a fixed period of separation, the apparent viscosity of a non-axisymmetric file is found to be higher than that of an axisymmetric file. In the case of non-axisymmetric motion, the apparent viscosity reaches a minimum at a certain ratio of the drop separation to tube radius. Drops with large effective radii to tube radius ratios develop slipper shapes, similar to those assumed by red blood cells in flow through capillaries, but only for capillary numbers in excess of a critical value.

1. Introduction

Motions of liquid drops, capsules, and cells through narrow channels and tubes with comparable dimensions arise in several natural, engineering, and physiological contexts. On the engineering side, we have liquid droplets of a binary mixture convected through the conduits of a porous medium in tertiary oil recovery (e.g. Olbricht 1996). On the biophysical side, we have red blood cells moving through the narrow branches of the capillary network in the microcirculation or through the bronchial airways (e.g. Skalak, Özkaya & Shalak 1989). In both cases, a desire to understand the factors that affect the individual drop motion, and to quantify its consequence on the global properties of the fluid, motivates a detailed investigation under the magnifying glass of microhydrodynamics. Further objectives depend on the

particular context; in the case of blood flow, understanding the factors that influence the red-blood-cell membrane tank-treading motion has been an important goal.

Two considerations complicate the analysis of flow in the presence of a drop or capsule in its general form. First, the interfacial mobility allows a flow to be established in the interior of the particle in response to the imposed flow due to an external shearing motion or pressure drop; this necessitates the kinematic and dynamic coupling of the interior and exterior flows taking into account the mechanical properties of the interface. Secondly, the interfacial deformability allows a drop to obtain a broad range of non-spherical transient shapes that must be computed simultaneously along with the rest of the variables that characterize the flow. Examples are the parachute and slipper-like shapes assumed by drops that are positioned off the centreline of a cylindrical tube.

Revoking the interfacial mobility, the interfacial deformability, or both, yields simplified systems involving rigid particles and spherical drops. Such systems have been studied extensively, and the results have provided us with complementary insights into the cardinal problem involving deformable drops. For example, Hyman & Skalak (1972*a*, *b*) computed the flow due to an axisymmetric file of nearly spherical drops moving along the centreline of a circular tube, regarding it as a model of blood flow. For fixed drop radius, they considered the motion as a function of the tube radius, drop separation, and viscosity ratio between the internal and ambient fluid. Their results showed that the deformed shapes are similar to those assumed by red blood cells moving through narrow glass tubes *in vitro*, or through blood vessels *in vivo*. Recent reviews and further results on the motion of drops and solid particles through tubes were presented by Hirschfeld, Brenner & Falade (1984), Higdon & Muldowney (1995), Sugihara-Seki (1996), Olbricht (1996), and Coulliette & Pozrikidis (1996). The recent resurgence of interest is partly due to the availability of efficient numerical methods that render extensive parametric investigations feasible, while requiring only moderate computational facilities.

The more challenging problem involving highly deformable drops moving through circular tubes has also been considered on several occasions. The theoretical analyses and numerical simulations, however, have been conducted under some important assumptions regarding the position or size of the suspended drops. Ho & Leal (1975) conducted an investigation of the axisymmetric motion of large drops whose equivalent diameter is comparable to the tube diameter; Chi (1986) extended the results to intermediate-sized drops. Martinez & Udell (1990) computed the axisymmetric motion of highly deformable drops in pressure-driven Stokes flow. Pozrikidis (1992) considered the corresponding problem of gravity-driven for a periodic array of drops. Borhan & Mao (1992) studied the effect of variable surface tension due to a surfactant, and Bozzi *et al*. (1997) investigated the effect of fluid inertia. Barthés-Biesel and coworkers (Leyrat-Maurin & Barthés-Biesel 1994; Queguiner & Barthés-Biesel 1997) studied the passage of liquid capsules through constrictions, cylindrical and tapered tubes. Other studies are reviewed by Olbricht (1996). Several authors investigated the motion and deformation of a drop above a plane wall, which approximates the motion of a small drop moving near the surface of a cylindrical tube (e.g. Kennedy, Pozrikidis & Skalak 1994).

In this paper, we present a computational study on the pressure-driven motion of a periodic array of deformable liquid drops positioned off the centreline of an infinite cylindrical tube with circular cross-section, under conditions of Stokes flow. The drops are neutrally buoyant and the interfaces are devoid of surfactants and thus in a state of uniform tension. This investigation generalizes previous studies by relaxing the

assumptions regarding the drop size and position. The generalization, however, is not complete, as it does not include the effect of the ratio of viscosities of the drop and suspending fluid, λ. In developing the numerical method and carrying out the numerical computations, we set $\lambda = 1$. The reason is that, at the present time, a practical method of computing the motion for an extended period of time and with adequate accuracy when λ has an arbitrary value, is not available. In spite of this limitation, we are still left with an extensive parametric space whose exploration requires substantial effort with respect to numerical development and computation.

The numerical simulations are based on the boundary-integral method for Stokes flow. The formulation uses the periodic Green's function of the equations of Stokes flow in a domain that is bounded externally by a cylindrical tube. The properties and computation of this Green's function were discussed in a previous article (Coulliette & Pozrikidis 1996). This formulation allows us to express the velocity field simply as an integral over the surface of one drop in the periodic array. An alternative formulation employs a simpler Green's function, such as the Stokeslet, but the velocity field arises indirectly by solving an integral equation of the first kind over the tube surface, as explained by Higdon & Muldowney (1995). We find that if the Green's function is computed by tabulation and interpolation, as will be discussed in §3.1, the present approach has significant advantages, and we advocate its use in more general problems of drop motion in domains with arbitrary shapes, but only when the viscosity ratio is equal to unity. For other values of the viscosity ratio, the alternative approach with the simpler Green's function is probably more efficient: the need to tabulate and interpolate the stress tensor corresponding to the Green's function puts our approach at a disadvantage.

Much of the previous work on drop motion through a tube has been motivated by applications in biomechanics. Liquid drops are crude models of red blood cells whose motion is of paramount significance on the physiology of blood flow in the micro-capillaries (e.g. Skalak *et al.* 1989). Although the interface of a red blood cell is considerably more complex than that between two immiscible fluids, the common feature of deformability gives partial reason to extracting information on the former by studying the latter. Theoretical and computational studies of red blood cell motion through capillaries are reviewed by Secomb & Hsu (1993). The most advanced of these studies use the equations of lubrication flow to describe the motion of tightly fitting cells in narrow capillaries.

The motion of drops through circular tubes represents one facet of the more general and more physically relevant problem of motion through cylindrical tubes with arbitrary cross-sections. Non-circular cylindrical shapes and axisymmetric but undulated shapes arise in the physiological and engineering applications mentioned at the beginning of this introduction. For example, the blood capillaries are not smooth but bulge into the lumen to accommodate the cell nuclei of the endothelium, and atherosclerosis causes blood vessels to develop constrictions. Similarly, the conduits of a natural porous medium have random undulation. Tsai & Miksis (1994, 1997) computed axisymmetric motions of drops through constricted capillaries. Unfortunately, the loss of axisymmetry in the boundary geometry introduces considerable computational difficulties that require further developments in the implementation of the numerical method. Non-circular geometries have been the subject of only a limited number of theoretical studies in special asymptotic limits (Coulliette & Pozrikidis 1996).

2. Mathematical formulation

We consider the generally unsteady motion of a periodic array of drops separated by distance L through a tube with a circular cross-section of radius R, as depicted in figure 1. The Reynolds number is assumed to be sufficiently small that the flow both inside and outside the drop is governed by the equations of Stokes flow (e.g. Pozrikidis 1997). The drops consist of a Newtonian fluid and are bounded by interfaces with infinitesimal thickness, negligible mass, and constant surface tension γ. The motion is described in a Cartesian or polar cylindrical coordinate system with the x-axis along the length of the tube.

As a preliminary, we introduce the Green's functions of the Stokes equation for the velocity and stress denoted, respectively, as $\boldsymbol{G}^{TP}(\boldsymbol{x}, \boldsymbol{x}_0, \alpha)$ and $\boldsymbol{T}^{TP}(\boldsymbol{x}, \boldsymbol{x}_0, \alpha)$, corresponding to the geometry of the problem under consideration. Physically, $u_i(\boldsymbol{x}, \alpha) = 1/(8\pi\mu)\, G_{ij}^{TP}(\boldsymbol{x}, \boldsymbol{x}_0, \alpha)\, b_j$ is the velocity, and $\sigma_{ik}(\boldsymbol{x}, \alpha) = 1/(8\pi) = T_{ijk}^{TP}(\boldsymbol{x}, \boldsymbol{x}_0, \alpha)\, b_j$ is the stress at the point $\boldsymbol{x}$ induced by a singly periodic array of point forces with uniform strength $\boldsymbol{b}$. The point forces are located in the interior, and are arranged along the axis, of a circular tube of radius R, and are separated by the distance L. One of the point forces is located at the point $\boldsymbol{x}_0$. This velocity field is required to vanish when either the field point $\boldsymbol{x}$, or the singularity point $\boldsymbol{x}_0$ is placed at the cylindrical wall. The third argument of the Green's functions α is a dimensionless parameter, to be defined more precisely in equations (2.4), determining the axial pressure drop over a period and thus the axial flow rate.

The properties and computation of the Green's functions are discussed by Coulliette & Pozrikidis (1996). The numerical procedure involves solving an integral equation of the first kind for the boundary traction induced by the point forces over one period of the tube wall. The kernel of the integral equation is the Green's function of triply periodic flow, which is expressed in terms of rapidly converging Ewald sums. The integral equation is solved by discretizing the wall into cylindrical elements and then applying a standard collocation method. The numerical procedure is not specific to the circular cross-section, but may also be used to obtain the Green's function for a tube with an arbitrary cross-section, although not for a tube whose cross-section varies with axial position. The Green's function for flow within a cylindrical tube, a portion of which translates, may be computed by a similar, though slightly more involved, method.

Combining now the boundary integral representations of the flow inside and outside the drop, and requiring that the velocity remain continuous across the interface, we obtain the integral equation

$$u_j(\boldsymbol{x}_0; \alpha) = \frac{2}{1+\lambda}\left(u_j^P(\boldsymbol{x}_0) - \frac{1}{8\pi\mu}\int_D \Delta f_i(\boldsymbol{x})\, G_{ij}^{TP}(\boldsymbol{x}, \boldsymbol{x}_0; \alpha)\, \mathrm{d}S(\boldsymbol{x}) + \frac{1-\lambda}{8\pi}\int_D^{PV} u_i(\boldsymbol{x})\, T_{ijk}^{TP}(\boldsymbol{x}, \boldsymbol{x}_0; \alpha)\, n_k(\boldsymbol{x})\, \mathrm{d}S(\boldsymbol{x})\right), \quad (2.1)$$

where the point $\boldsymbol{x}_0$ lies in the interface (e.g. Pozrikidis 1992). The integrals are computed over the surface of one drop, denoted as D. The various symbols, variables, and parameters are defined as follows: μ is the viscosity of the suspending fluid, $\lambda\mu$ is the viscosity of the drops, and PV denotes the principal value of the improper double-layer integral. The density of the double-layer potential, $\Delta\boldsymbol{f}$, is the difference in the modified traction exerted on either side of the interface; for neutrally buoyant drops whose interfaces are devoid of surfactants, $\Delta\boldsymbol{f} = 2\gamma\kappa_m \boldsymbol{n}$, where κ_m is the mean

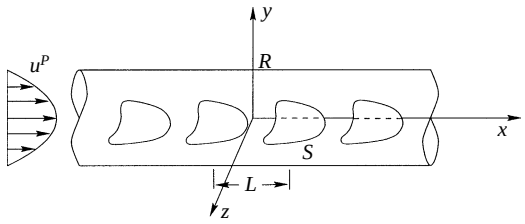

FIGURE 1. Schematic illustration of pressure-driven flow of a file of deformable drops through a circular tube.

curvature of the interface, γ is the surface tension, and $\boldsymbol{n}$ is the unit vector normal to the interface pointing into the suspending fluid. Finally, $\boldsymbol{u}^P = U_{cl}(1-\sigma^2/R^2)\,\boldsymbol{e}_x$ is the velocity of pressure-driven Poiseuille flow, σ is the radial position in cylindrical polar coordinates, R is the tube radius, U_{cl} is the centreline velocity, and $\boldsymbol{e}_x$ is the unit vector along the x-axis.

All boundary conditions are satisfied by the boundary-integral representation leading to equation (2.1). The condition of zero velocity at the tube surface, in particular, is guaranteed by the choice of the Green's function $\boldsymbol{G}^{TP}$. The use of any other Green's function would have resulted in integrals over the surface of the tube, integrals over cross-sections of the tube, or both, adding to the complexity of the integral equation and accompanying numerical method.

If the viscosity of the fluid inside the drop is equal to the viscosity of the ambient fluid, $\lambda = 1$, the coefficient of the double-layer integral vanishes, and we obtain an integral representation for the velocity,

$$u_j(\boldsymbol{x}_0;\alpha) = u_j^P(\boldsymbol{x}_0) - \frac{1}{8\pi\mu}\int_D \Delta f_i(\boldsymbol{x})\, G_{ij}^{TP}(\boldsymbol{x},\boldsymbol{x}_0;\alpha)\,\mathrm{d}S(\boldsymbol{x}). \tag{2.2}$$

This expression is valid when the point $\boldsymbol{x}_0$ is located in the interior, exterior, or at the surface of a drop. In the remainder of this paper, it will be tacitly assumed that $\lambda = 1$.

2.1. *Apparent viscosity*

The relative apparent viscosity of the suspension can be defined in terms of the negative pressure drop ΔP over a length L, and the axial volumetric flow rate Q, as

$$\frac{\mu_a}{\mu} = \frac{\Delta P}{L}\frac{\pi R^4}{8\mu Q}. \tag{2.3}$$

In the absence of the drops, μ_a/μ is equal to unity (e.g. Pozrikidis 1997, p. 184). More generally, the pressure drop and axial flow rate can be computed in terms of surface integrals over one drop using the formulae

$$\left.\begin{aligned} \Delta P &= \frac{4\mu U_{cl} L}{R^2} + \alpha\frac{2}{\pi R^2}\int_D \Delta f_x(\boldsymbol{x})\,(R^2-\sigma^2)\,\mathrm{d}S(\boldsymbol{x}), \\ Q &= \tfrac{1}{2}\pi U_{cl} R^2 + (1-\alpha)\frac{1}{4\mu L}\int_D \Delta f_x(\boldsymbol{x})\,(R^2-\sigma^2)\,\mathrm{d}S(\boldsymbol{x}), \end{aligned}\right\} \tag{2.4}$$

(Coulliette & Pozrikidis 1996). The first term on the right-hand side of each of these equations corresponds to the unperturbed parabolic flow. The significance of the dimensionless parameter α that first appears in (2.1), the arguments of the Green's

function, is now evident. When $\alpha = 0$, the disturbance pressure drop due to the drops vanishes, and the total pressure drop is equal to that of the unperturbed flow; when $\alpha = 1$, the disturbance flow rate due to the drops vanishes, and the axial flow rate is equal to that of the unperturbed flow. Any intermediate choice is acceptable, but does not admit a simple physical interpretation.

In the numerical simulations, we set $\alpha = 1$, thus considering a flow that is pumped at a constant flow rate. Fluctuations in the pressure drop reflect the transient deformation of the drops. The transient motion for a constant-flow-rate flow can be significantly different to that for a constant pressure-drop flow corresponding to $\alpha = 0$, and it is not clear how one can be deduced from the other. For example, the start-up flow of a single fluid in a tube, subject to a constant flow rate, begins with a plug-flow velocity profile, whereas the start-up flow subject to a constant pressure-drop accelerates smoothly from zero velocity (e.g. Pozrikidis 1997). Assuming that the flow rate and the pressure drop are properly matched, both profiles tend to the same steady fully developed profile at long times. The steady motion for a constant-flow-rate flow can be inferred from that for a constant pressure-drop flow and *vice versa* provided that the capillary numbers are properly matched.

The deformability of the drops can be expressed by the capillary number Ca, which is the ratio of the typical magnitude of the viscous stresses and the surface tension. Since the former scale with $\mu V/R$ and the latter with γ/a, we define $Ca = \mu Va/\gamma R$; V is the mean velocity of the fluid given by $V = Q/\pi R^2 = \frac{1}{2}U_{cl}$. Martinez & Udell (1990) use the alternative capillary number $\mu V/\gamma$, which does not involve the drop size; this is an appropriate choice for axisymmetric motion. The present choice is more appropriate for the purposes of our investigation, as the capillary number remains meaningful in the limit of low concentrations where each drop finds itself immersed in a virtually unbounded unidirectional shear flow and its ability to deform is in direct proportion to its size.

3. Numerical procedure

The numerical procedure follows the standard steps of a boundary-element method with certain new features. Some are specific to the particular problem under consideration, and others are of a more general interest.

3.1. *Tabulation and interpolation of the Green's function*

The numerical computation of the integral on the right-hand side of equation (2.2) requires a multitude of evaluations of the Green's function $\boldsymbol{G}^{TP}$. Each evaluation using the boundary-element method developed by Coulliette & Pozrikidis (1996) consumes a prohibitively large amount of time, approximately 6 s on a SUN SPARCstation 20 workstation with a 50 MHz processor running at 99 % capacity.

To reduce this computation cost, we tabulate the polar cylindrical components of a non-singular complementary component of the Green's function, denoted as $\boldsymbol{J}(\boldsymbol{x}, \boldsymbol{x}_0)$, and then reconstruct them by interpolation. Similar procedures were followed by Loewenberg & Hinch (1996) and Li, Charles & Pozrikidis (1996) for a doubly or triply periodic flow. Specifically, we set $\boldsymbol{J}(\boldsymbol{x}, \boldsymbol{x}_0) = \boldsymbol{G}^{TP}(\boldsymbol{x}, \boldsymbol{x}_0) - \boldsymbol{S}(\boldsymbol{x}, \boldsymbol{x}_0) + \boldsymbol{S}(\boldsymbol{x}, \boldsymbol{x}_0^R)$, where $\boldsymbol{S}(\boldsymbol{x}, \boldsymbol{x}_0)$, is the three-dimensional Stokeslet, $\boldsymbol{x}$ is the field point, $\boldsymbol{x}_0$ is the singular point, and $\boldsymbol{x}_0^R$ is the reflection of $\boldsymbol{x}_0$ through the tube wall. Subtracting $\boldsymbol{S}(\boldsymbol{x}, \boldsymbol{x}_0) - \boldsymbol{S}(\boldsymbol{x}, \boldsymbol{x}_0^R)$ from $\boldsymbol{G}^{TP}(\boldsymbol{x}, \boldsymbol{x}_0)$ yields smooth functions that are amenable to standard interpolation. Other complementary Green's functions were tested, but the chosen one produced the most accurate results with the least amount of CPU time.

In constructing the interpolation tables, we let the independent variables scan the nodes of a uniform grid on the four-dimensional space of $(x-x_0, \sigma, \sigma_0, \quad - \quad _0)$, where $x-x_0$ varies in $[0, L]$, σ, σ_0 vary in $[0, R]$, and $\quad - \quad _0$ varies in $[0, \pi]$. The polar cylindrical components of the complementary Green's function between grid points are computed by quadra-variate linear interpolation, and the corresponding Cartesian components are recovered by a simple orthogonal transformation. We used 20 interpolation points for $x-x_0$, 10 points for σ and σ_0, and 30 points for $\quad - \quad _0$. For $L/R = 2$, this gives nearly equal intervals between interpolation points in each variable. In this case, the average absolute error tested over a sample of 1000 randomly chosen positions for $\boldsymbol{x}$ and $\boldsymbol{x}_0$ was of the order of 10^{-3}. Generating a grid of this size requires computing the Green's function at 60000 points of the aforementioned parametric space, and consumes 81 h on the available computer facilities. This may appear as an excessive computational cost, but the Green's function is tabulated only once for each periodic drop separation, and then fully exploited in the parametric investigations. Storing a table of the aforementioned size in binary form requires only 4320 Kb of memory. The Green's function tables are available on request.

The change in volume of a drop is a measure of the accuracy of the numerical simulation. We found that the change in volume increases as the periodic separation between the drops is reduced, even though, with a constant number of interpolation points, the interpolation points with respect to $x-x_0$ becomes more dense. It appears that the rapid variation of the velocity field overcompensates the reduction of the interpolation error. With the exception of the computations presented in §7 for $L/R = 1$, the final volume change of the drops was less than 3% through a simulation.

The interpolation error is compounded to the numerical error introduced by computing the grid values of the Green's function using the boundary-element method. The maximum magnitude of the latter occurs as either the field point or the observation point approaches the wall. The overall error is reduced substantially by forcing $\boldsymbol{G}^{TP}$ to vanish at the wall at the stage of interpolation. With this modification, the maximum relative error in the computation $\boldsymbol{G}^{TP}$ occurs at $\sigma/R = 0.9$, and is of the order of 2%.

3.2. *Implementation of the boundary-integral method*

To describe the initially spherical shape of a drop, we consider a regular octahedron comprised of eight equilateral triangular sides, and then make a sequence of successive divisions, each time dividing a triangular base into four descendant triangles and thus quadrupling the number of sides. Each element is defined by six marker points, three located at the vertices and three at the middle of its edges. Finally, the vertices and mid-points of the edges are projected onto the sphere to yield an unstructured grid. The number of elements N increases at the rate of $N = 8 \times 4^m$, where m is an integer indicating the level of discretization. The total number of vertices and mid-nodes is $2N+2$. A FORTRAN program that performs this discretization and generates a connectivity table is available on request. The connectivity table gives, among other quantities, the numbers of the elements that host a particular node, and the numbers of the nodes that define a particular element.

The shape of the elements is described in a parametric manner in terms of two local surface coordinates (ξ, η) that map the position vector of a point in the interior of an element to a point within a right-angled triangle in the (ξ, η) plane; the corresponding mapping functions are given by Pozrikidis (1998). The right-angle of the parameter triangle is located at the origin of the parameter plane, and the lengths of its two equal sides are equal to unity. The normal vector and mean curvature over the triangle are

computed using this parametric representation and standard formulae of differential geometry (e.g. Pozrikidis 1997, pp. 16, 21).

The unit normal vector at a particular marker point has a multitude of values computed from the parametric representation of the elements that share the point. For example, the unit normal vector at the mid-points has two values. The numerical error is reduced drastically by setting the normal vector at each point equal to an unweighted average of all pertinent values, and then computing it in the interior of an element by quadratic interpolation with respect to the local surface coordinates.

The single-layer integral over the interfacial elements is computed using a triangle integration rule (e.g. Pozrikidis 1998). The singularity is ameliorated by expressing the variables of integration in plane polar coordinates with the origin at the singular point.

The interface is symmetric with respect to the plane that passes through the drop centroid and the tube axis. Thus, even though all nodes must be stored or reproduced by reflection during the evaluation of the interfacial integrals, the velocity at only about half of the nodes is necessary. To ensure the flawless performance of the numerical method, however, the symmetry was exploited only in a limited number of cases. The round-off error caused the nodes that lie in the plane of symmetry to be lifted by a small distance by the end of a simulation, thereby suggesting that the symmetric motion is stable.

3.3. *Advancing the interface*

After the interfacial velocity has been computed at the marker points, the position of the marker points is advanced using a standard time-integration method, as will be described later in this section. If the velocity of the marker points is set equal to the velocity of the fluid $\boldsymbol{u}$ given in equation (2.2), the marker points tend to migrate rapidly toward the rear of the drop, causing numerical instabilities and a dilapidation of the interface. One way of preventing this catastrophe, is to replace the tangential component of the fluid velocity, $\boldsymbol{n}\times\boldsymbol{u}\times\boldsymbol{n}$, with a multiple of the tangential component of the velocity of the volume-centroid of the drop, $f(\sigma)\,\boldsymbol{n}\times\boldsymbol{U}\times\boldsymbol{n}$; the volume-centroid $\boldsymbol{x}_c$ is computed in terms of a surface integral over the interface, $\boldsymbol{x}_c = 1/(2V)\int \boldsymbol{n}\,\boldsymbol{x}\cdot\boldsymbol{x}\,\mathrm{d}S$, where V is the drop volume. The centroid velocity $\boldsymbol{U}$ arises by backward numerical differentiation. The dimensionless modulating function $f(\sigma)$ reduces the magnitude of the tangential velocity near the tube, and increases it near the tube centreline, in a manner that is consistent with the velocity profile of the unperturbed Poiseuille flow. A good choice for $f(\sigma)$ is $f(\sigma) = (R^2-\sigma^2)/(R^2-\sigma_c^2)$, where σ_c is the radial position of the drop centroid; an even better choice is $f(\sigma) = (R^2-(\zeta\sigma-\zeta\sigma_c+\sigma_c)^2)/(R^2-\sigma_c^2)$ where ζ is an empirical constant. Numerical experimentation suggested setting $\zeta = [|\boldsymbol{u}\cdot\boldsymbol{n}|_{max}/(U_{cl}(1-\sigma_{c0}^2/R^2))]^2$, where σ_{c0} is the initial radial position of the drop centroid. This expression adjusts the magnitude of the tangential component of the marker-point velocity so that it is less than that of the parabolic flow near the quasi-steady state. A similar but more involved method was used by Loewenberg & Hinch (1996) in their study of multiple-drop motion in a periodic flow. A more sophisticated method was developed by Zinchenko, Rother & Davis (1997).

The interface is advanced by integrating the system of ordinary different equations that determines the motion of the marker points, using the adaptive Runge–Kutta–Fehlberg method RFK23 (e.g. Pozrikidis 1998), which requires three velocity evaluations for each marker point per timestep. The additional evaluation required in comparison with the standard second-order Runge–Kutta method allows the interface to evolve slowly during the most interesting phases of the deformation, and rapidly during the less interesting phases of the deformation.

Using the procedure described in §3.1 for the tabulation and interpolation of

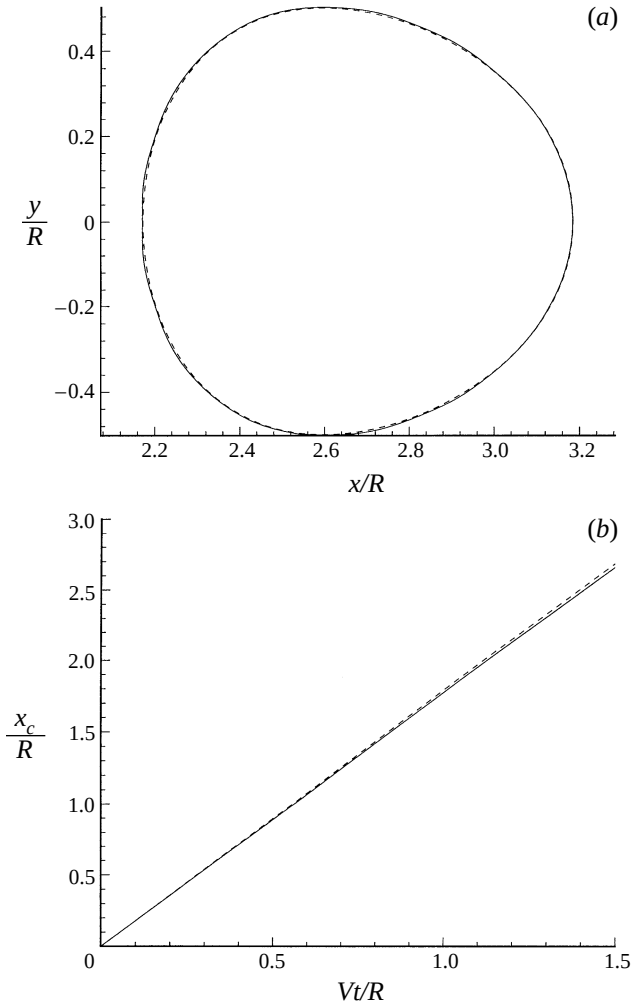

FIGURE 2. Comparison of results obtained using - - -, a boundary-integral method for axisymmetric flow, and ——, the present method for three-dimensional flow, for drop separation $L/R = 3$, drop radius $a/R = 0.5$, and capillary number $Ca = 0.10$; (*a*) quasi-steady shapes after an evolution time $Vt/R = 1.5$, where V is the mean velocity of the unperturbed flow; (*b*) axial position of the drop centroid.

the Green's function, the adaptive time-stepping method, and the aforementioned procedure to control the quality of the grid, we obtain an overall successful numerical method. For small drops, 128 elements are sufficient to resolve the interface shape, whereas for large drops, 512 elements are necessary; 39.6 s per timestep for 128 elements and 9.24 min per timestep for 512 elements are required on the available computer facilities. In all studies discussed in the following sections, 60–100 timesteps were sufficient for the drops to reach a quasi-steady state, or for the motion to proceed up to a time of $Vt/R = 1.5$. For a drop with 512 elements, running the executable code requires 16–236 Kb of memory, including the storage of the Green's function.

4. Parametric investigation and code validation

Several non-dimensional parameters affect the motion of the drops, including the reduced effective drop radius a/R, the capillary number $Ca = \mu Va/\gamma R$, the reduced initial radial position of the drop centroid σ_{c0}/R, and the reduced separation L/R. To facilitate the presentation of the results, we consider separately small drops with $a/R < 0.5$, and large drops with $a/R > 0.5$. The parameters studied in each category are restricted to those that have the most significant influence. In the case of small drops, these are the reduced effective drop radius a/R and the capillary number Ca. In the case of large drops, these are the reduced initial radial position of the centroid σ_{c0}/R and the capillary number Ca. In determining the effect of periodic separation, we simultaneously investigate the combined effect of initial radial position and periodic separation.

Martinez & Udell (1990) and Pozrikidis (1992) computed axisymmetric motions of deformable drops through a cylindrical tube. The former considered the steady pressure-driven motion of one drop, and the latter considered the transient buoyancy-driven motion of a periodic file of drops. We extended the method of Pozrikidis (1992) to make it applicable to pressure-driven flow, and thus obtained a computer code that was used to validate the present results for three-dimensional flow.

In figure 2, we compare results computed by the method for axisymmetric flow, and those computed by the present method for three-dimensional flow, for a periodic file of drops with separation $L/R = 3$, drop radius $a/R = 0.5$, and capillary number $Ca = 0.10$. In figure 2(*a*), we present the shape of a quasi-steady drop, and in figure 2(*b*) we present the transient axial position of the centroid of one drop in the array. The results of the two computations are in excellent agreement. Note, in particular, that the drop shape has a higher curvature at the front than at the back, which is consistent with previous theoretical predictions and laboratory observations (Goldsmith & Mason 1963; Hyman & Skalak 1972*b*; Ho & Leal 1975). The motion of the surrounding fluid was first analysed by Hyman & Skalak (1972*a*) who found that when the drop spacing is greater than about one tube diameter, a bolus of suspending fluid is trapped between each pair of successive drops. This behaviour is reproduced by our numerical method.

5. Small drops

Consider a particular drop belonging to a file of drops, moving off the tube centreline. If the drop is sufficiently small, the parabolicity of the Poiseuille-flow velocity profile may be neglected, and the incident flow may be approximated with a single shear flow having an appropriate shear rate. The effect of the tube may also be neglected to a leading-order approximation. Taylor (1934) showed that when the capillary number is sufficiently small, a drop in steady simple shear flow with velocity $\boldsymbol{u} = G(y - y_c)\boldsymbol{e}_x$, where G is the constant shear rate, deforms into a ellipsoid whose aspect ratio and inclination relative to the direction of flow are functions of the capillary number $Ca_{SSF} = \mu Ga/\gamma$ and of the viscosity ratio λ.

Using the shear rate of the Poiseuille flow at the centroid of the drop, $G_c = \partial u_x^P/\partial\sigma$, we define the local capillary number

$$Ca_l = \frac{\mu|G_c|a}{\gamma} = \frac{2\mu a U_{cl}\,\sigma_c}{\gamma R^2} = 4\frac{\sigma_c}{R}Ca, \tag{5.1}$$

where $Ca = \mu Va/\gamma R$. The local capillary number permits comparisons of drop behaviours in simple shear flow and pressure-driven tube flow.

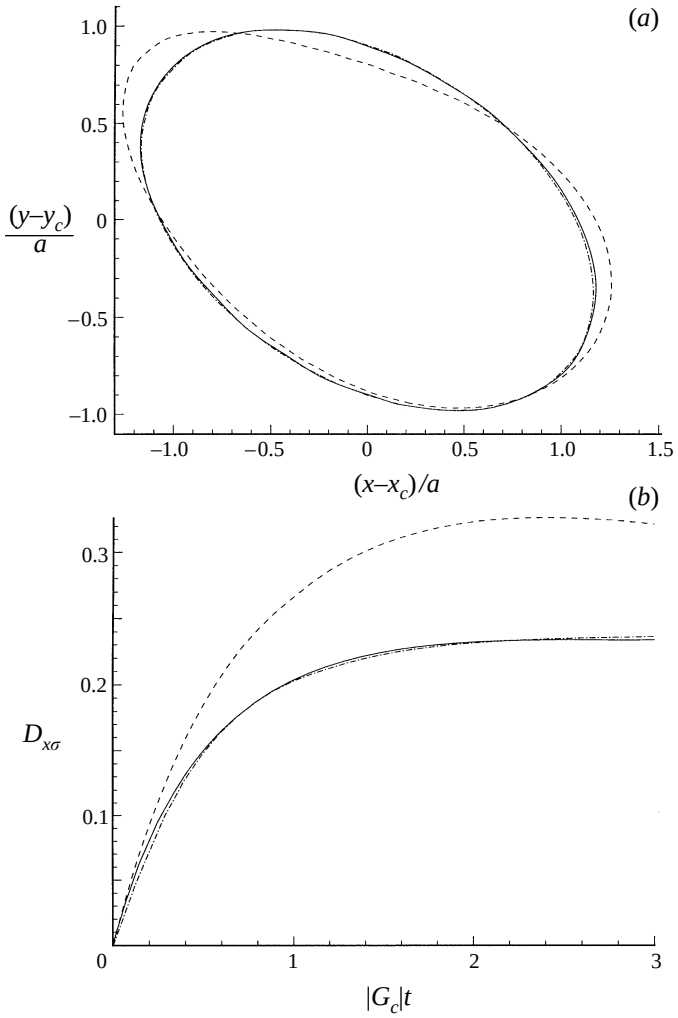

FIGURE 3. (*a*) Mid-plane profiles of quasi-steady drops in a period file with $L/R = 2$, initial radial position $\sigma_{c0}/R = 0.50$, $a/R = 0.1$ and 0.4, and $Ca = 0.10$, compared with the profile of a drop in simple shear flow with capillary number Ca_{SSF} equal to the local capillary number $Ca_l = 0.2$. (*b*) The corresponding transient deformation parameter. ——, $a/R = 0.1$; ---, 0.4; –·–, simple shear flow.

In figure 3(*a*), we present the steady profile of a drop in simple shear flow in the plane of symmetry that is perpendicular to the vorticity vector of the unperturbed flow for $Ca_{SSF} = 0.20$, along with quasi-steady profiles of drops with $a/R = 0.1$ and 0.4 in pressure-driven tube flow, for $\sigma_c/R = 0.5$ and $Ca = 0.10$ corresponding to $Ca_l = Ca_{SSF} = 0.20$. The tube centreline is located beneath the depicted profiles. The drop with radius $a/R = 0.1$ is nearly identical to that of a drop in simple shear flow, but the drop with $a/R = 0.4$ is significantly more elongated, and has an egg-like shape. The change in shape as the drop size is increased is due to the more prominent effect of the variation in the shear rate with respect to the radial distance, with high values near the tube wall and low values near the centreline, but also to the presence of the wall. Larger drops deform more severely at the region adjacent to the wall than near the centreline.

The magnitude of the drop deformation can be described in terms of the

deformation parameter $D = (c-b)/(c+b)$; c and b are the maximum and minimum dimensions of the drop in the azimuthal plane passing through the drop centroid. Figure 3(*b*) illustrates the deformation of a drop in a simple shear flow, compared to that of drops with radii $a/R = 0.1$ and 0.4 in pressure-driven tube flow, corresponding to figure 3(*a*). The asymptotic deformation of a drop in simple shear flow is nearly identical to that of the small drop in Poiseuille flow. As observed earlier, the deformation of the large drop is significantly more pronounced. Overall, these results indicate that it is safe to use the approximation of locally simple shear flow when a/R is as high as 0.10 and perhaps even somewhat higher.

5.1. *Migration and quasi-steady shapes*

Next, we consider the radial drop migration and the establishment of quasi-steady shapes. Two factors influence the drop deformation and thus migration in tube flow, including the parabolicity of the Poiseuille velocity profile, and the presence of the wall.

The first factor was considered in detail by Chan & Leal (1979), who derived the following expression for the trajectory of a drop in infinite parabolic flow:

$$\frac{\sigma_c^2-\sigma_{c0}^2}{2R^2}+\left(1-\frac{2\lambda}{2+3\lambda}\frac{a^2}{R^2}\right)\ln\frac{\sigma_{c0}}{\sigma_c}=-(x_c-x_{c0})\frac{U_{cl}\,a^3\mu}{R^4\gamma}q(\lambda), \tag{5.2}$$

where

$$q(\lambda)=\frac{2\lambda}{(1+\lambda)^2(2+3\lambda)}\left[\frac{3}{14}\frac{16+19\lambda}{2+3\lambda}(2\lambda^2+\lambda-1)+\frac{10+11\lambda}{140}(3\lambda^2-\lambda+8)\right]. \tag{5.3}$$

Numerical evaluation gives $q(\lambda = 1) = \frac{9}{20}$.

The influence of the wall can be estimated using the results of the small-deformation theory for flow past a drop above a plane wall. Following the analysis of Shapira & Haber (1990) and the discussion of Kennedy *et al.* (1994), we argue that the rate of migration of a drop that is located far from a wall, $R-\sigma_c \gg a$, and far from the tube centreline, $\sigma_c \gg a$, is given by

$$\frac{\mathrm{d}\sigma_c}{\mathrm{d}t}=-|G_c|\frac{a^3}{(R-\sigma_c)^2}g(\lambda)\,D_T, \tag{5.4}$$

where D_T is the Taylor deformation parameter of a drop that is suspended in infinite simple shear flow at capillary number $Ca_{SSF} = Ca_l$. Chan & Leal (1979) derived the expression

$$g(\lambda)=\frac{3}{280}\frac{54\lambda^2+97\lambda+54}{(1+\lambda)^2}. \tag{5.5}$$

Under the aforementioned restrictions on the drop size, shape, and position, we expect that equation (5.4) will approximately describe the radial migration of a drop in the presence of a tube wall. From figure 2, we note that the longitudinal position of the drop centroid is a nearly linear function of time, so we may substitute the relation $\mathrm{d}x_c = \eta V\,\mathrm{d}t$ into equation (5.4), where η is the observed slope, and evaluate the shear rate at the drop centroid in terms of the radial position of the centroid, to find

$$\frac{\mathrm{d}\sigma_c}{\mathrm{d}x_c}=-\frac{4\sigma_c}{\eta R^2}\frac{a^3}{(R-\sigma_c)^2}g(\lambda)\,D_T. \tag{5.6}$$

Using the boundary-integral method, we computed the deformation parameter D for a periodic file of drops in a tube, applied a least-squares regression to find η, and

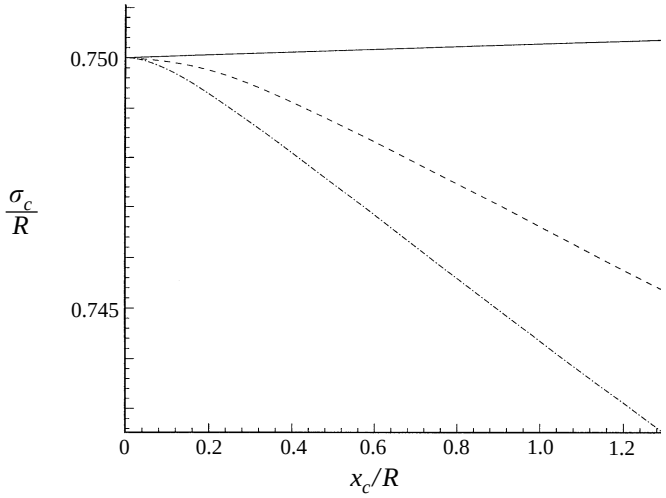

FIGURE 4. Trajectory of drop centre with initial radial position $\sigma_{c0}/R = 0.75$, radius $a/R = 0.1$, and $Ca = 0.10$, predicted by the parabolic-flow theory of Chan & Leal (1979) corresponding to the solid line, the present numerical method corresponding to the dashed line, and the small-deformation wall-migration theory discussed in the text corresponding to the dash-dot line.

integrated the ordinary differential equation (5.6) using the fourth-order Runge–Kutta method, with D_T on the right-hand side replaced by D.

In figure 4, we present the trajectory of a drop centroid computed from equations (5.2) and (5.6), and the actual trajectory arising from our numerical method for initial drop position $\sigma_{c0}/R = 0.75$, drop radius $a/R = 0.1$, and $Ca = 0.10$. For $\lambda = 1$, the theory of Chan & Leal (1979) predicts migration toward the wall, whereas the small-deformation theory resulting in equation (5.6) predicts rapid migration away from the wall. Our numerical results fall between these two extremes. Considering the underlying assumptions, equation (5.6) offers reasonable predictions. Unfortunately, we are not aware of any experimental data for flow in a tube with $\lambda = 1$ that can be used to confirm our predictions. Nonetheless, it is worth noting that the analysis of Chan & Leal (1979) predicts lower migration rates than those observed in the experiments of Goldsmith & Mason (1963) for $\lambda \ll 1$, and this provides us with a partial explanation for the discrepancies in figure 4.

Since the drop migration velocity is small, it is appropriate to characterize the motion in terms of two timescales: the time it takes for a drop to deform from an initial spherical shape to a nearly steady shape, T_{Def}, and the time it takes for a drop to migrate a radial distance comparable to the drop radius, T_{Mig}. Kennedy *et al.* (1994) showed that T_{Def} may be estimated from the results of the transient small-deformation theories for unbounded shear flow, and the timescale T_{Mig} may be estimated from equation (5.4). Following their arguments, we set

$$T_{Def} = \frac{\lambda Ca}{|G_c|}, \quad \frac{1}{|G_c|\, g(\lambda) D}\left(\frac{R-\sigma_c}{a}\right)^3, \tag{5.7}$$

and define

$$\tau \equiv \frac{T_{Def}}{T_{Mig}} = Ca\,\lambda\, g(\lambda)\, D\left(\frac{a}{R-\sigma_c}\right)^3. \tag{5.8}$$

When $Ca \ll 1$ and $R-\sigma_c \gg a$, equation (5.8) gives $\tau \ll 1$; the drops reach quasi-steady

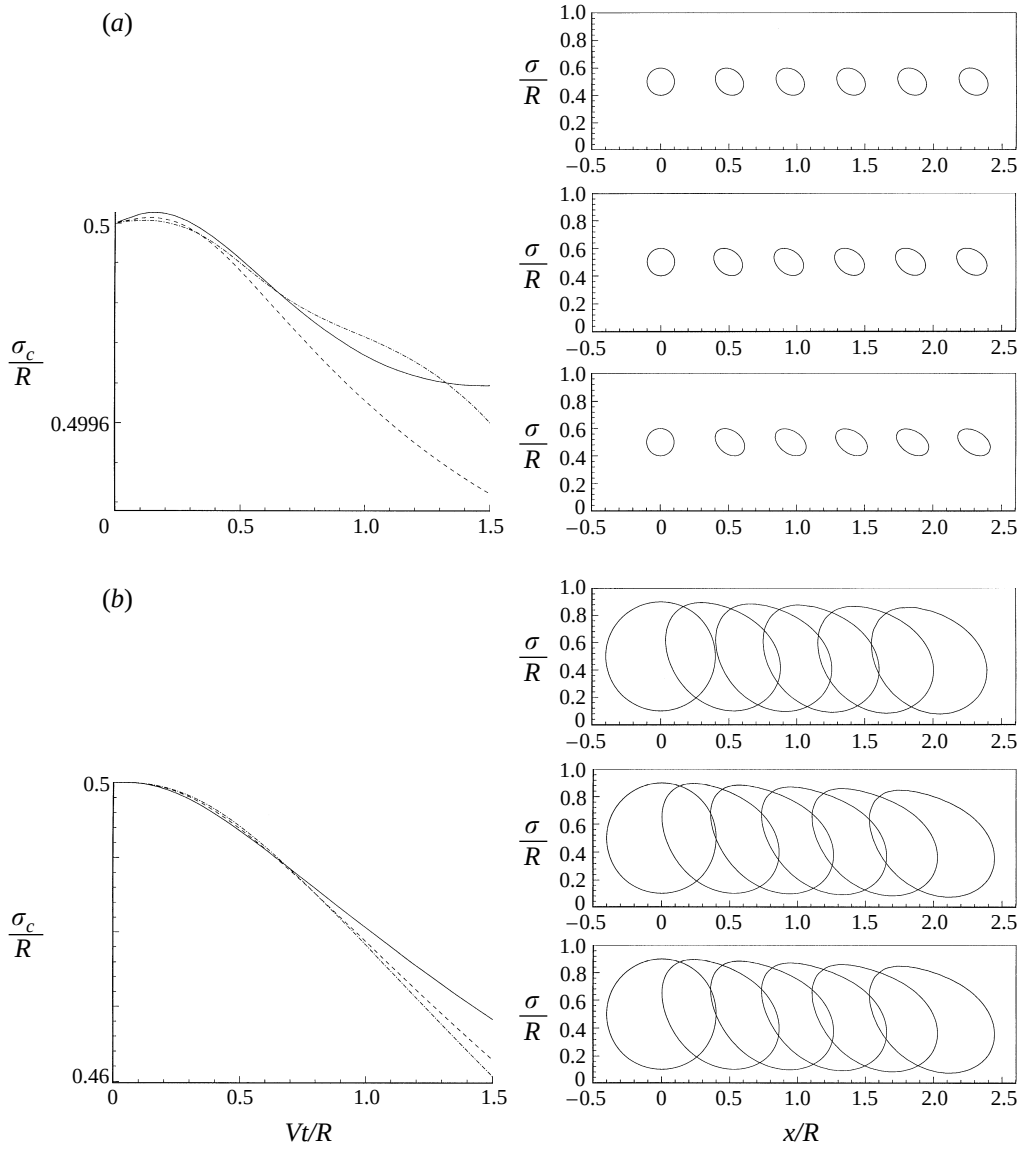

FIGURE 5. Radial position of the drop centroid, and transient profiles of a drop at $Vt/R = 0$, 0.3, 0.6, 0.9, 1.2 and 1.5 for $L/R = 2$, $\sigma_{0c}/R = 0.5$, and reduced drop radius (*a*) $a/R = 0.1$, (*b*) 0.4. ——, $Ca = 0.050$; ---, 0.075; –·–, 0.100.

shapes whereupon the deformation is the exclusive cause of the inward migration. In all cases to be discussed in the remainder of this subsection, these two conditions are met. In the computations, the drops were considered to have obtained quasi-steady shapes when $(\boldsymbol{u}-\boldsymbol{U})\cdot\boldsymbol{n}/V$ is of the order of 10^{-2}.

To illustrate the effect of the capillary number, on the left-hand side of figure 5 we plot the radial position of the drop centroid, and on the right-hand side we plot the corresponding transient shapes at $Vt/R = 0$, 0.3, 0.6, 0.9, 1.2 and 1.5, for $L/R = 2$, $\sigma_{c0}/R = 0.5$, $Ca = 0.05$, 0.075 and 0.1, and $a/R = 0.1$ and 0.4. In both cases, $a/R = 0.1$ and 0.4, after an initial transient period, the drops migrate toward the centreline.

For the smaller drops with $a/R = 0.1$, there is an initial start-up period during which

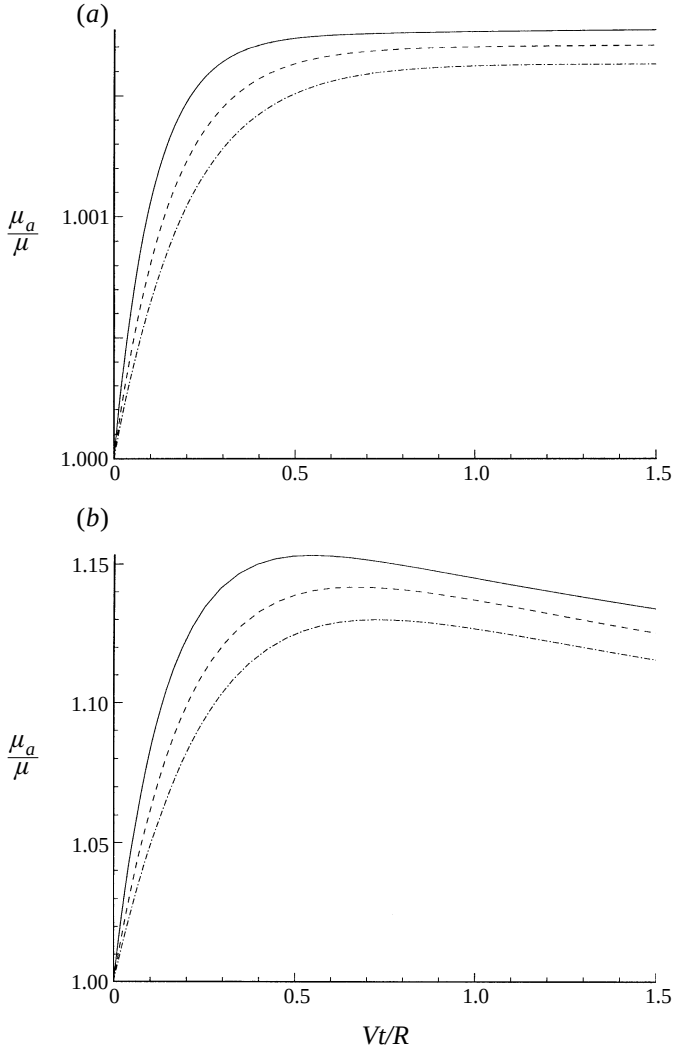

FIGURE 6. Relative apparent viscosity of the suspension for $L/R = 2$, $\sigma_{0c}/R = 0.5$, and reduced drop radius (*a*) $a/R = 0.1$, (*b*) 0.4. ——, $Ca = 0.050$; ---, 0.075; –·–, 0.100.

the centroids appear to move slightly away from the centreline. When the rate of initial deformation lessens, the drops begin migrating towards the centreline. However, the magnitude of the radial displacement is very small, and it is possible that the wall-bound motion is merely a numerical artifact. There are no visible differences in shapes between $Vt/R = 0.3$ and 0.6, confirming that the drops have indeed reached quasi-steady shapes at an early time.

In contrast, there are significant differences in the shapes of the drops with $a/R = 0.4$ at $Vt/R = 0.3$ and 0.6, as shown in figure 5(*b*). The shapes become quasi-steady by the time $Vt/R = 0.9$. There are still slow changes in shape after that time, but they are due to the radial migration and the resultant tendency of the drops to reach the centreline. Since the deformation of an axisymmetric drop is less than that of a deformed drop located off the centreline, it follows that maximum deformation should occur after a finite evolution time. Indeed, the deformation of parameter reaches

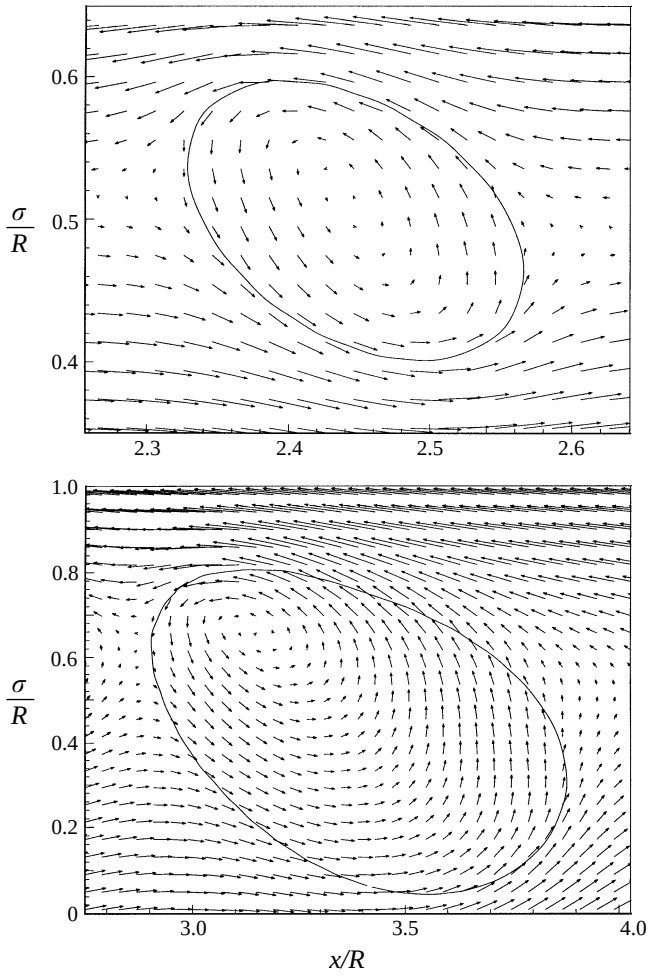

FIGURE 7. Velocity vectors interior and exterior to a quasi-steady drop in the plane passing through the drop centroid and the tube axis, in a frame of reference translating axially with the drop centroid, for $L/R = 2$, $\sigma_{0c}/R = 0$, capillary number $Ca = 0.1$, and reduced drop radius (*a*) $a/R = 0.1$, (*b*) 0.4.

a maximum, and then it decreases linearly as the drop exhibits significant radial migration.

5.2. *Apparent viscosity*

In figure 6 we plot the relative apparent viscosity for $L/R = 2$, $\sigma_{c0}/R = 0.5$, $a/R = 0.1$, 0.4, and for three values of the capillary number. If both cases $a/R = 0.1$, 0.4, the apparent viscosity shows a rapid initial increase, as the drops are adjusting to the environment, and then it changes at a lower rate. For $a/R = 0.4$, the apparent viscosity reaches a maximum, and then it shows a linear decline caused by the inward migration of the drops towards the centreline. Thus, minimum energy dissipation occurs when the drops move along the centreline, and the apparent viscosity is a monotonic function of the distance from the centreline.

Gaehtgens (1987) reported that the off-centre positioning of red blood cell files in horizontal tubes, caused by sedimentation, significantly increases the apparent viscosity of the blood. These experimental observations agree with the linear decrease in figure 6(*b*) at long times. Sugihara-Seki & Skalak (1988) computed the relative apparent

viscosity of a two-dimensional suspension containing a single file of freely suspended rigid circular cylinders of radius $a/H = 0.4$ and separation $L/H = 2$; H is the channel half-width and a is the equivalent cylinder radius. They also found that the apparent viscosity increases as the radial position of the file is made larger. It is important to note, however, that the periodic array is not necessarily stable in its axisymmetric state, that is, an energetically favourable state is not necessarily stable to disturbances that displace the drops in a subharmonic way.

5.3. *Flow field*

In figure 7, we present velocity vector fields in the azimuthal plane passing through the drop centroid for $L/R = 2$, $\sigma_{c0}/R = 0.5$, $Ca = 0.1$, and $a/R = 0.1$ and 0.4, in a reference frame moving with the drop centroids. In both cases, the fluid near the tube centreline moves faster than the drops, whereas the fluid near the tube wall moves slower than the drops. A counterclockwise eddy develops in the drop interiors. The streamlines in the mid-plane are not necessarily closed, but form spiral patterns reflecting the three-dimensional structure of the flow. The centre of the eddy inside the drop with $a/R = 0.1$ nearly coincides with the drop centroid, but the centre of the eddy for $a/R = 0.4$ is located closer to the wall.

In the intervening region between the drops with $a/R = 0.4$ shown in figure 7(*b*), there is a point where both components of the fluid velocity nearly vanish, indicating that a bolus of fluid has been established and travels with the drops. A similar bolus was identified in previous studies of axisymmetric flow (Hyman & Skalak 1972*a*) and was also observed in intercellular plasma motion between red blood cells travelling through narrow capillary tubes (Gaehtgens, Duhrssen & Albrecht 1980). There is a large variation in the magnitude of the axial velocity near the edge of the bolus close to the wall. In contrast, the axial component of the velocity varies in a smooth parabolic manner between the small drops shown in figure 7(*a*), and this indicates that a travelling bolus does not develop. For a bolus to form, the spacing between the drops must be greater than about one tube diameter, and the effective radius of the drops must be of the same order as the tube radius. When these conditions are not met, the streamlines join smoothly at the rear of a travelling drop.

6. Large drops

When the drops are sufficiently large, the undeformed interfaces intersect the tube centreline, and the capillary number is sufficiently high, an evolving dimple may develop at the rear of the drops, and the drops may assume a slipper shape, as shown in figure 8 for drops with $L/R = 2$, $\sigma_{c0}/R = 0.05$, $a/R = 0.7$, $Ca = 0.4$, at $Vt/R = 1.5$. Figure 8(*a*) illustrates the drop surface represented by a grid of 512 quadratic elements, each subdivided into four planar elements for better display; figure 8(*b*) shows the same file with the surfaces displayed using Gouraud shading. A similar slipper shape has been observed in numerous experimental studies of red-blood-cell flow.

In figure 9(*a*), we present microphotographs of red blood cells circulating in the mesentery of a dog (after Fung 1969), and in figure 9(*b*) we present microphotographs of red blood cells travelling in a single file through a 6.2 μm capillary tube after Gaehtgens *et al.* (1980). There is a general similarity between the drop shapes formed by the periodic file shown in figure 8 and those of the red blood cells displayed in the photographs. It should be pointed out, however, that the drops develop a slipper-like shape only when the capillary number is in excess of the critical value, whereas the red blood cells appear to do so always, as long as the tube radius is sufficiently small.

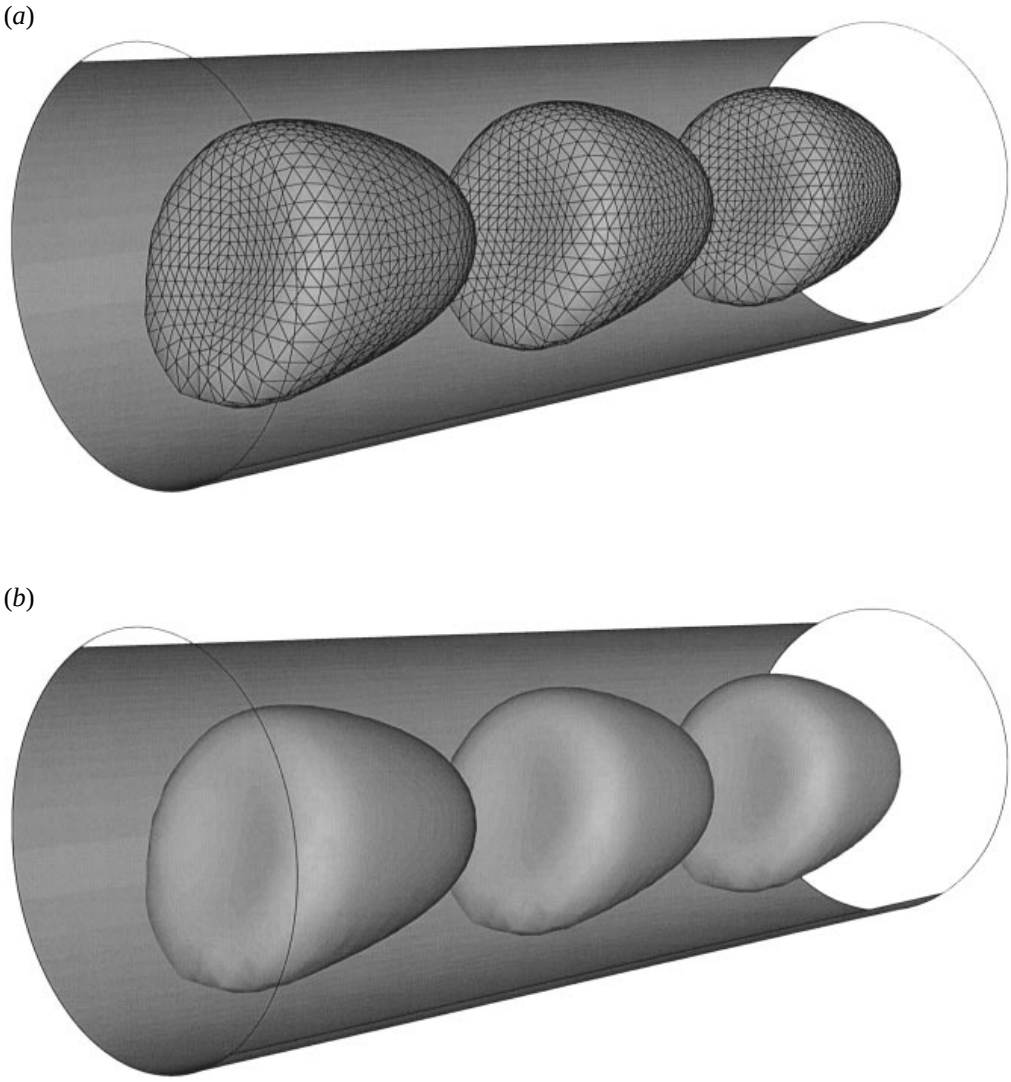

FIGURE 8. Slipper-shaped drops at $Vt/R = 1.5$ for $L/R = 2$, $\sigma_{0c}/R = 0.05$, $a/R = 0.7$, and $Ca = 0.4$, showing the drop surface displayed with (*a*) a grid of 512 quadratic elements each subdivided into four planar elements, (*b*) Gouraud shading.

Conditions under which the drops develop dimples and then maintain them could not be found; instead, the ambient fluid keeps invading the drop interior, possibly reaching their fronts; our computations became unreliable well before that point owing to the inadequate spatial resolution. Thus, there is an important difference between red blood cells and liquid drops. Owing to the incompressibility of the interfaces, the red blood cells are able to sustain the slipper shape, whereas the drops deform in an unrestricted manner possibly leading to break-up (Pozrikidis 1992; Olbricht & Kung 1992; Tsai & Miksis 1994).

In figure 10, we compare profiles of drops at time $Vt/R = 1.5$, for $L/R = 2$, $a/R = 0.7$, $Ca = 0.40$, and $\sigma_{c0}/R = 0$, 0.05, 0.10 and 0.15. The shapes of the rear portions of the interfaces are notably sensitive to the initial radial position. In particular, as σ_{c0}/R

(*a*)

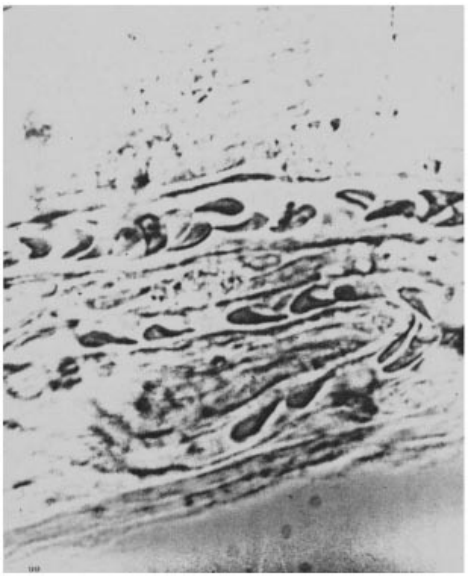

(*b*)

FIGURE 9. (*a*) Microphotographs of red blood cells circulating in the mesentery of a dog (Fung 1969); (*b*) microphotographs of red blood cells travelling in single file through a 6.2 μm capillary tube (Gaehtgens *et al.* 1980).

is increased, the near surfaces become more elongated and the dimple becomes less pronounced, eventually disappearing at a critical off-centre distance. Thus, a dimple will develop only if the drops are sufficiently close to the centreline and the capillary number is sufficiently high. For $\sigma_{c0}/R = 0.15$, a small ripple is observable at the lower lateral surface nearest the tube wall, owing to the numerical error associated with the element skewness.

In figure 11, we illustrate the radial migration of the drops shown in figure 10. Initially, all drops are placed below the centreline. The centroids of all drops start moving toward the wall as the drop is adjusting to its environment, but then they pause and begin migrating towards the centreline. As σ_{c0}/R is increased, the initial period during which the drop centroids move away from the centreline becomes longer. For example, when $\sigma_{c0}/R = 0.10$ or 0.15, the drops start migrating toward the centreline when $Vt/R = 0.85$ or 1.43. This observation suggests a criterion for computing the critical capillary number below which the drops are able to reach a quasi-steady shape without developing a dimple. A capillary number may be considered to be less than the critical value when the drops establish a nearly constant migration velocity toward the centreline after a finite evolution time. Our results confirm that the critical capillary number is a function of the initial radial position of the drops. We found empirically that $Ca_{cr} = 0.25R/(R+\sigma_{c0})$. Since the capillary number was defined to be proportional to a/R, a drop is less likely to reach a quasi-steady state when it is large, or when it is initially positioned far from the centreline.

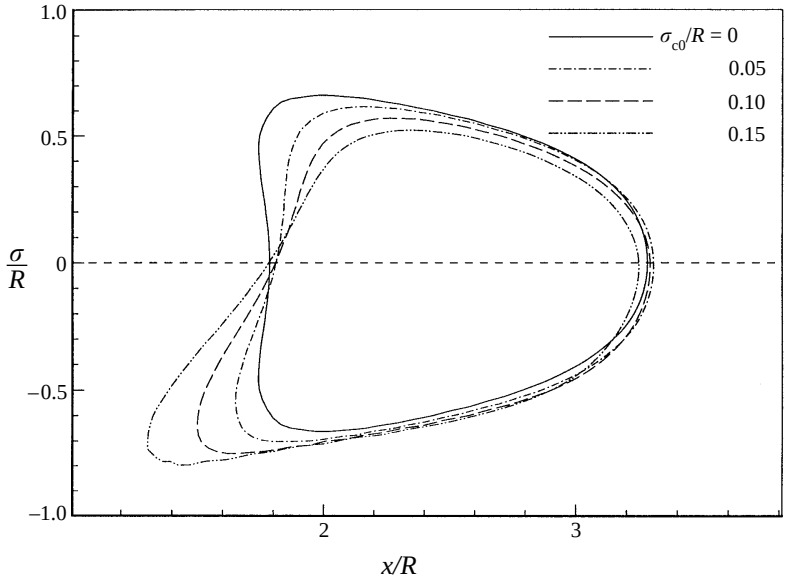

FIGURE 10. Comparison of drop shapes at approximately $Vt/R = 1.5$ for $L/R = 2$, $a/R = 0.7$, $Ca = 0.40$, and initial drop position $\sigma_{0c}/R = 0$, 0.05, 0.10 and 0.15.

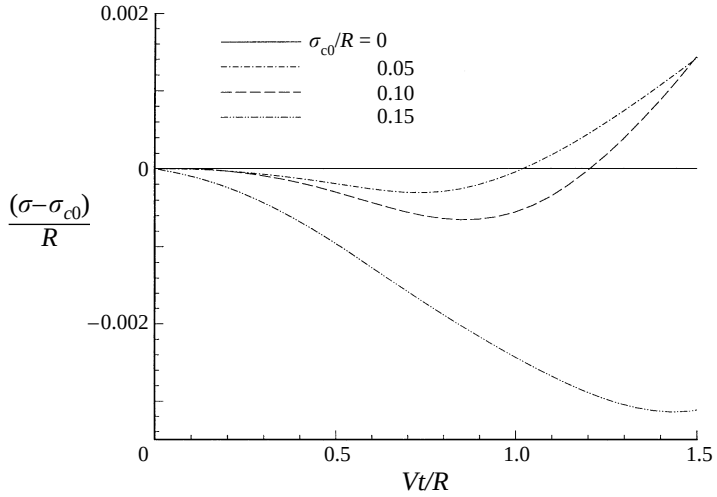

FIGURE 11. Radial position of the drop centroid for the cases displayed in figure 10.

6.1. *Apparent viscosity*

In figure 12, we present the relative apparent viscosity of the suspension depicted in figure 10. As the initial radial position of the drop centroid is increased, the apparent viscosity increases in a manner that is similar to that discussed previously for small drops. A new feature is that none of the apparent viscosity curves presented in figure 12 tend to become linear at long times, as was noted for small drops with $a/R = 0.1$ or 0.4. This difference is probably due to the large magnitude of the capillary number for large drops. For all cases presented in figure 12, the ratio of timescales τ discussed

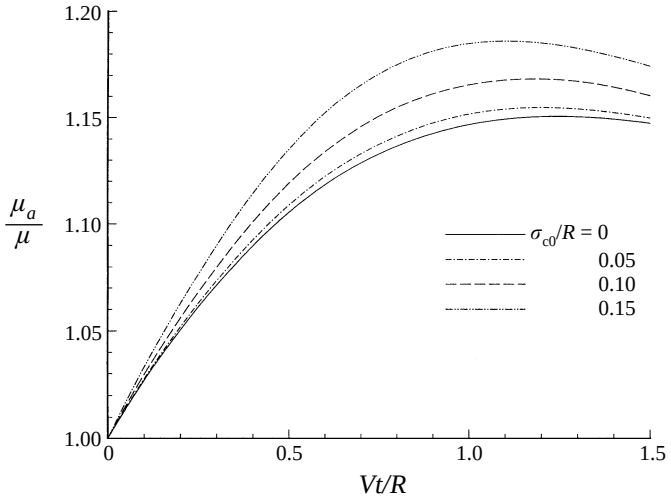

FIGURE 12. Relative apparent viscosity of the suspension for the cases displayed in figure 10.

in the preceding section is significantly larger than unity. The viscous-induced stresses caused by the pressure-driven flow are large in comparison to surface tension, and the deformation continues without an apparent approach to a quasi-steady shape.

We performed a set of computations similar to those corresponding to figure 12 for smaller capillary numbers. A dimple did not form in the near of the drop, and the apparent viscosity curves did tend to become a linear function of time, at long times.

6.2. *Flow field*

It is revealing to examine the structure of the flow field over the interfaces. In figure 13 we present interfacial streamlines over slowly evolving drops at $Vt/R = 1.5$, for $L/R = 2$, $a/R = 0.7$, $Ca = 0.40$, and $\sigma_{c0}/R = 0.05$ and 0.10, in a frame of reference moving with the drop centroid. The interfacial streamlines were computed from the tangential component of the velocity, neglecting the normal motion. The tube wall is moving backward relative to the slowly evolving drops. There is a stagnation point at the leading tip, and an open dividing streamline at the front surface of each drop; the latter extends towards the rear of the interface along the part that is adjacent to the wall and then closes at a rear stagnation point. At the front upper side of the drops, there is a clear distinction between the back-flow of suspending fluid and the bolus of fluid between the drops; at the front lower side where the dividing streamline turns back, the distinction is not as clear. The non-axisymmetry of the file of drops shown in figure 13(*b*) is more pronounced than that shown in figure 13(*a*). Correspondingly, the rear stagnation point is further away from the centre of the dimple. Martinez & Udell (1990) observed a similar flow pattern over a solitary axisymmetric drop, including a circular dividing surface streamline that completely encircles the front of the drop.

In figure 14, we plot the velocity vector field corresponding to figure 13(*a*). The slower moving fluid near the tube wall transmits strong shear stresses across the interface and causes the onset of a toroidal eddy in the interior. The flow toward the rear of the drop occurs predominantly in a shell adjacent to the interface, whereas the compensating flow towards the front occurs through a jet directed along the centreline. This interior flow pattern is similar to that described by Martinez & Udell (1990) for a solitary axisymmetric drop.

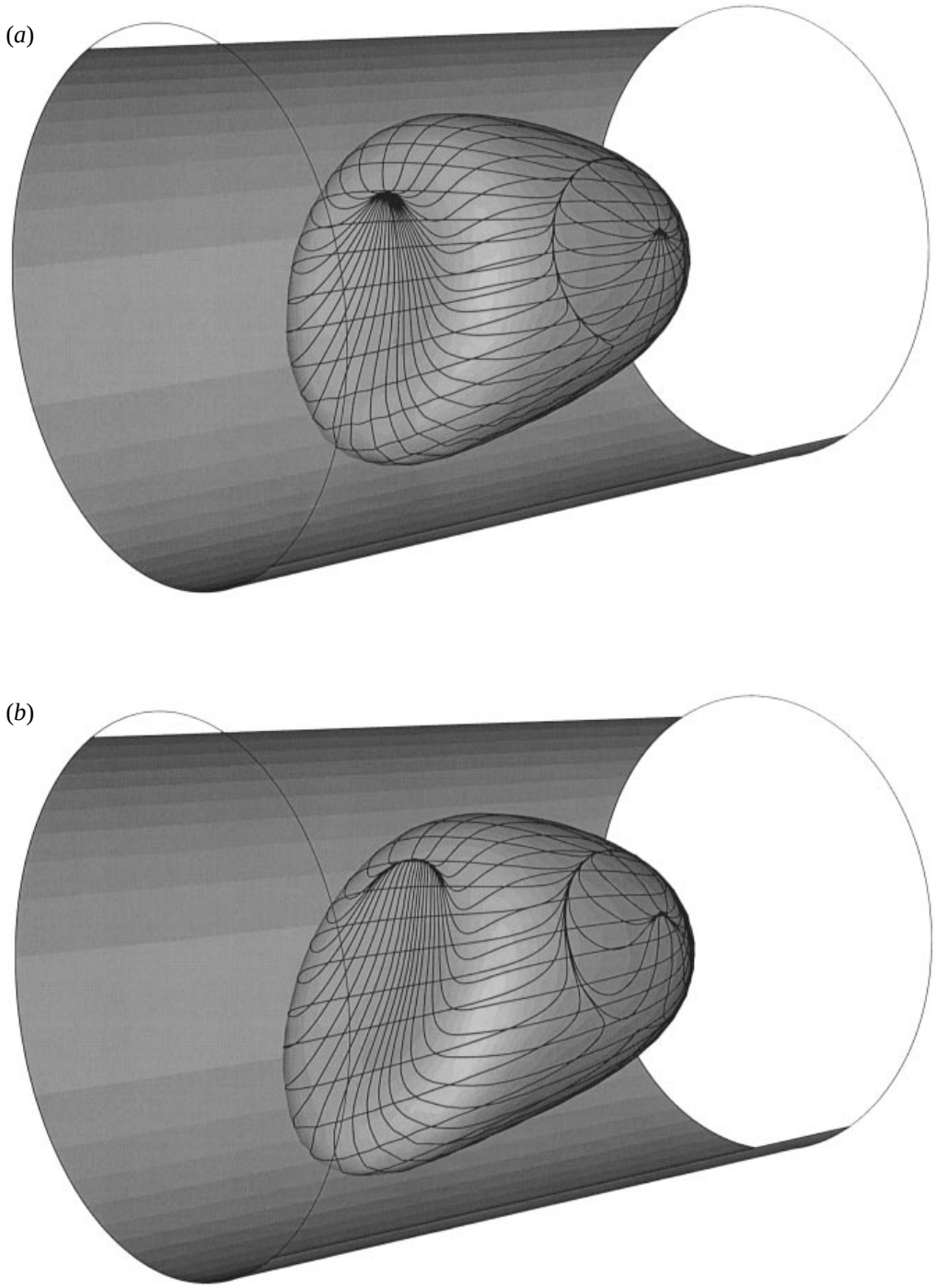

FIGURE 13. Interfacial streamlines at $Vt/R = 1.5$ for $L/R = 2$, $a/R = 0.7$ and $Ca = 0.40$, and initial drop position (*a*) $\sigma_{0c}/R = 0.05$, (*b*) 0.10.

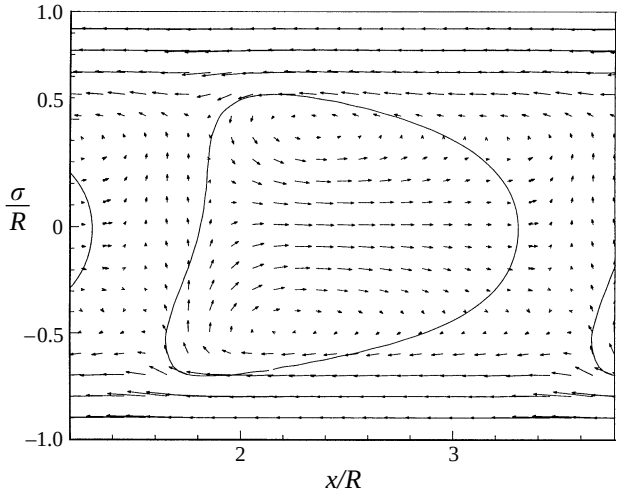

FIGURE 14. Velocity vectors interior and exterior to a drop in the plane passing through the drop centroid and the tube axis, in a frame of reference translating axially with the centroid of the drop at $Vt/R = 1.5$ for $L/R = 2$, $a/R = 0.7$, $Ca = 0.40$ and $\sigma_{0c}/R = 0.05$.

7. Effect of drop separation

As a last topic, we examine the effect of reduced drop separation L/R on the shape of quasi-steady drops, fixing the value of the capillary number. In figure 15(a, b), we present shapes for $a/R = 0.4$, $\sigma_{c0}/R = 0.5$, $Ca = 0.05$, and $L/R = 2.0$, 2.5 and 3.0. In all cases, the drop centres are located sufficiently far from the tube centreline so that the interfaces do not develop dimples regardless of the magnitude of the capillary number. There are noticeable but small differences in the shapes of the drops with $L/R = 2$ and $L/R = 2.5$, and more significant differences between the shapes of drops with $L/R = 2.5$ and $L/R = 3.0$. The deformation parameter for the three cases shown are, respectively, equal to 0.136, 0.158 and 0.360. Since the disturbance flow due to a drop effectively vanishes a few tube radii upstream and downstream from its centre, the drops for $L/R = 3$ are affected only mildly by their neighbours, and we expect that a further increase in L/R will cause only small changes. Unfortunately, our inability to compute the Green's function for large separations with sufficient accuracy prevented us from confirming this assertion.

The drop separation has a significant influence on the apparent viscosity of the suspension. In figure 16, we present the time evolution of the apparent viscosity for $a/R = 0.4$, $L/R = 2.0$, 2.5 and 3.0, and $\sigma_{c0}/R = 0$, 0.1, 0.25 and 0.5. For axisymmetric drops, described in figure 16(a), the apparent viscosity decreases as the periodic separation becomes larger. In contrast, figures 16(b)–16(d) show a non-monotonic dependence for non-axisymmetric motion. After the quasi-steady state has been established, the arrangement has a minimum apparent viscosity when $L/R = 2.5$, and this value is insensitive to the initial radial position.

To resolve the physical reason of this non-monotonic behaviour, we used a numerical method similar to that described by Zhou & Pozrikidis (1994) to compute the apparent viscosity of a period file of two-dimensional drops in a channel of half width equal to H, for reduced equivalent drop radius $a/H = 0.4$, initial drop distance from the centreline $y_c/H = 0.5$, $Ca = 0.05$, and separation $L/H = 2.0$, 2.5 and 3.0. We found that the apparent viscosity decreases monotonically with the periodic separation. A similar monotonic behaviour was reported by Sugihara-Seki & Skalak (1988) for an

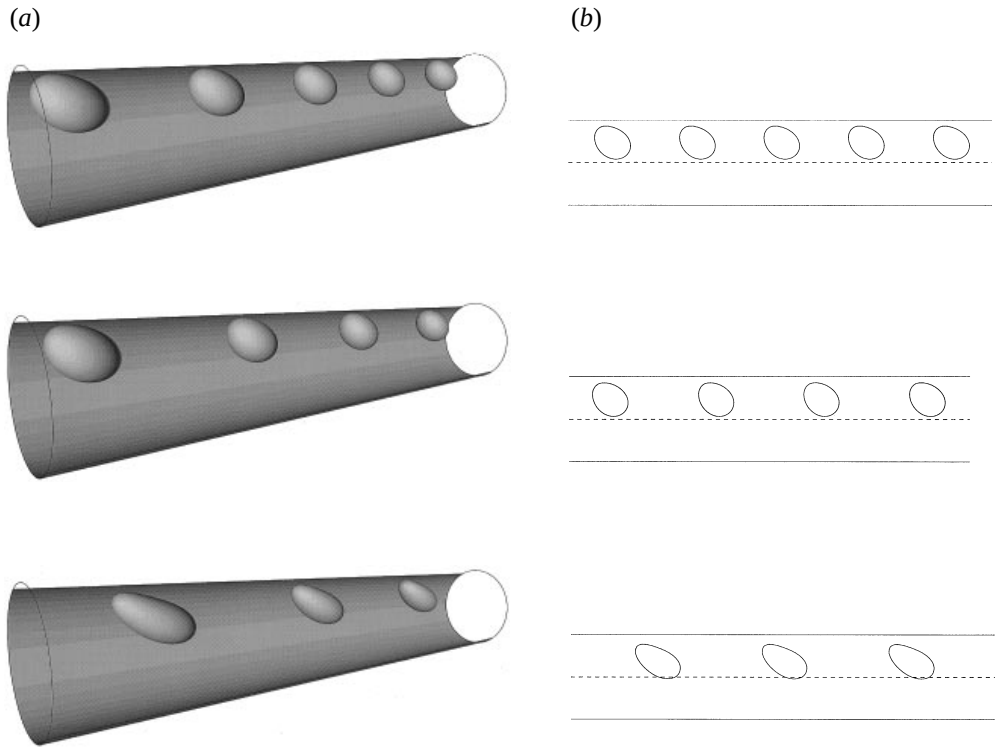

FIGURE 15. Quasi-steady drops for $a/R = 0.4$, $Ca = 0.05$, and $\sigma_{0c}/R = 0.5$, for $L/R = 2$, 2.5 and 3. (*b*) Corresponding profiles in the plane passing through the drop centroid and the tube axis.

off-centre file of rigid cylindrical particles. It appears then that the existence of a minimum apparent viscosity at certain periodic separations is a distinguishing feature of the three-dimensional flow.

We mentioned that minimum apparent viscosity occurs when $L/R = 2.5$ regardless of the initial radial position. This can be seen more clearly in figure 17(*a*) where we plot the apparent viscosity caused by quasi-steady drops at $Vt/R = 1.5$, against the drop separation, for $\sigma_{c0}/R = 0$, 0.1, 0.25 and 0.5, corresponding to the conditions of figure 16. The error bars were determined from the volume change between the initial and final state at $Vt/R = 1.5$. As the flow becomes increasingly more axisymmetric, the variation of the apparent viscosity with periodic separation tends to become monotonic. We expect that for each initial radial position, as L/R is made larger, the apparent viscosity will asymptotically approach a value corresponding to a solitary drop.

Further insights into the effect of separation on the apparent viscosity can be gained be varying the drop size, while keeping the capillary number and initial position of the file constant. In figure 17(*b*), we plot the apparent viscosity against the separation for quasi-steady drops with sizes $a/R = 0.10$, 0.25, 0.33 and 0.40. As the drop radius is increased, the variation of the apparent viscosity with separation becomes increasingly less monotonic. Thus, increasing the separation causes the apparent viscosity of a quasi-steady file to be reduced, provided that the drops are sufficiently small or close to the centreline. Unfortunately, we are not aware of experimental results on the apparent viscosity of a file with $\lambda = 1$ that show either the decreasing of the apparent

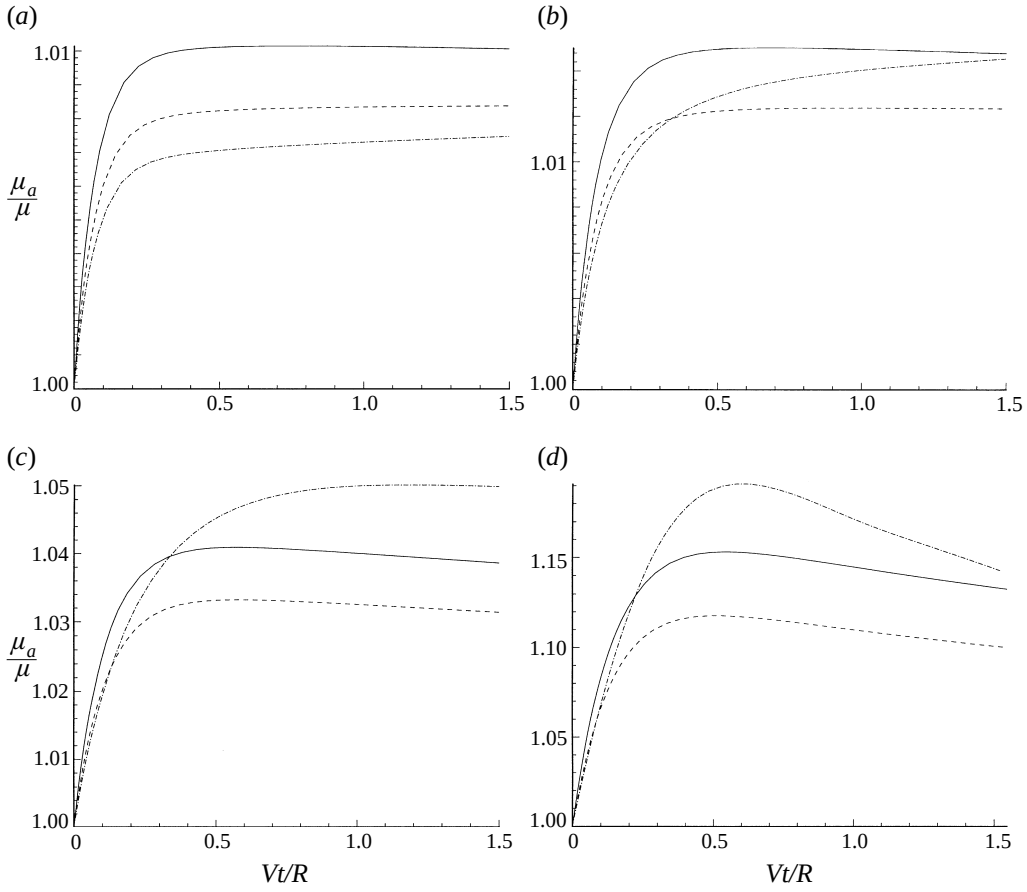

FIGURE 16. Effect of drop separation on the relative apparent viscosity for $a/R = 0.4$, $Ca = 0.05$ and ——, $L/R = 2$; ---, 2.5; –·–, 3; (*a*) $\sigma_{0c}/R = 0$, (*b*) 0.1, (*c*) 0.25, (*d*) 0.5.

viscosity with increasing periodic separation, or the occurrence of the minimal apparent viscosity at a finite separation.

8. Discussion

We found that, after an initial adjustment period, the drops migrate toward the centreline. When the capillary number is sufficiently low, a quasi-steady state is established where changes in the drop shape are caused predominantly by the radial migration. The quasi-steady shapes are affected significantly by the distance of the off-centre arrangement from the centreline and the drop separation.

The stability of the motion of the single file of deformable drops has not been considered. Sugihara-Seki & Skalak (1988) investigated the stability of single and dual rows of rigid circular cylinders spaced regularly in a two-dimensional channel. Their results showed that when the initial position is slightly perturbed from the staggered, two-file configuration, the cylinders execute oscillatory motion around their steady positions. In contrast, the single file and the symmetric double file are unstable. Sugihara-Seki, Skalak & Secomb (1990) investigated the stability of a staggered arrangement of triangular cells, and Secomb & Hsu (1993) investigated the stability of

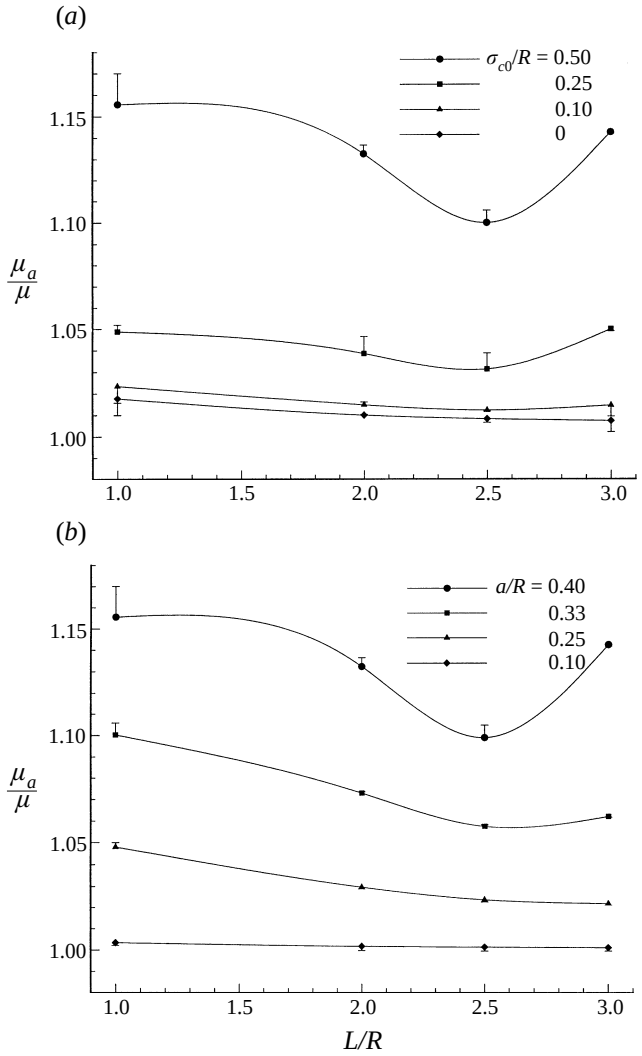

FIGURE 17. Effect of drop separation on the relative apparent viscosity at $Vt/R = 1.5$ for $Ca = 0.05$, and (*a*) $a/R = 0.4$, (*b*) $\sigma_{0c}/R = 0.5$.

rigid closely fitting particles, with similar findings. Red blood cells rarely arrange themselves in perfectly regular single or double files (Gaehtgens 1980; Gaehtgens *et al.* 1980), and deformable liquid drops at high concentrations are likely to show similar behaviours.

Close inspection of figure 8(*a*) reveals that the interfacial elements are larger in the higher curvature regions at the rim of the dimple than at the centre. This unfortunate distribution is due to our inability to effectively control the quality of the grid by dynamically adjusting the velocity of the nodes comprising the vertices of the triangular elements. To achieve the highest possible accuracy with a given number of elements, smaller elements in the regions of higher curvature are required, but not so small as to impose strong constraints on the size of the timestep. Zinchenko *et al.* (1997) developed a grid-controlling algorithm by placing restrictions of the variations of the inter-node distances and minimizing the rate of change of these distances. We

are currently implementing the advancing front method described by Nakahashi & Sharov (1995) for directly triangulating a curved surface in the physical space. This method allows for a precise control of the triangle size and skewness by monitoring local variations of curvature, and incorporates a facility for adaptive refinement (Hinton, Rao & Ozakca 1991). The result is a discretization that requires a minimal number of elements and maintains a consistently accurate representation of the interfaces for longer evolution times.

This research was supported by the National Science Foundation and the Sun Microsystems Corporation. Acknowledgment is made to the donors of the Petroleum Research Fund, administered by the American Chemical Society, for partial support. Computing time on a CRAY C90 was provided by the San Diago Supercomputer Centre. The authors thank Richard Skalak, J. M. Rallison, Saroja Ramanujan, Madhu Gopalakrishnan, Xiaofan Li, and Keiko Nomura, for comments on various aspects of this research.

REFERENCES

Borhan, A. & Mao, C.-F. 1992 Effect of surfactants on the motion of drops through cylindrical tubes. *Phys. Fluids* A **4**, 2628–2640.

Bozzi, L. A., Feng, J. Q., Scott, T. C. & Pearlstein, A. J. 1997 Steady axisymmetric motion of deformable drops falling or rising through a homoviscous fluid in a tube at intermediate Reynolds number. *J. Fluid Mech.* **336**, 1–32.

Chan, P. C.-H. & Leal, L. 1979 The motion of a deformable drop in a second-order fluid. *J. Fluid Mech.* **92**, 131–170.

Chi, B. K. 1986 The motion of immiscible drops and the stability of annular flow. PhD thesis, Cal. Inst. Tech.

Coulliette, C. 1996 Motion of drops through tubes. PhD thesis, University of California, San Diego.

Coulliette, C. & Pozrikidis, C. 1996 Flow due to a periodic array of point forces, and the motion of small particles within a cylindrical tube of arbitrary cross-section. *Phys. Fluids* **8**, 2019–2031.

Fung, Y. 1969 Blood flow in the capillary bed. *J. Biomech.* **2**, 353–372.

Gaehtgens, P. 1980 Flow of blood through narrow capillaries: Rheological mechanisms determining capillary hematocrit and apparent viscosity. *Biorheology* **17**, 183–189.

Gaehtgens, P. 1987 Tube flow of human blood at near zero shear. *Biorheology* **24**, 367–376.

Gaehtgens, P., Duhrssen, C. & Albrecht, K. H. 1980 Motion, deformation, and interaction of blood cells and plasma during flow through narrow capillary tubes. *Blood Cells* **6**, 799–812.

Goldsmith, H. L. & Mason, S. G. 1963 The flow of suspensions through tubes: Single large bubbles. *J. Colloid Sci.* **18**, 237–261.

Higdon, J. J. L. & Muldowney, G. P. 1995 Resistance functions for spherical particles, droplets and bubbles in cylindrical tubes. *J. Fluid Mech.* **298**, 193–210.

Hinton, E., Rao, N. V. & Ozakca, M. 1991 Mesh generation with adaptive finite element analysis. *Adv. Engng Software* **13**, 238–262.

Hirschfeld, B. R., Brenner, H. & Falade, A. 1984 First- and second-order wall effects upon the arbitrarily-shaped, -positioned and -oriented particle within a circular cylinder. *PhysicoChem. Hydrodyn.* **5**, 999–133.

Ho, B. P. & Leal, L. G. 1975 The creeping motion of liquid drops through a circular tube of comparable diameter. *J. Fluid Mech.* **71**, 361–384.

Hyman, W. & Skalak, R. 1972*a* Non-Newtonian behavior of a suspension of liquid drops in tube flow. *AIChE J.* **18**, 149–154.

Hyman, W. & Skalak, R. 1972*b* Viscous flow of a suspension of liquid drops in a cylindrical tube. *Appl. Sci. Res.* **26**, 27–52.

Kennedy, M. R., Pozrikidis, C. & Skalak, R. 1994 Motion and deformation of liquid drops, and the rheology of dilute emulsions in simple shear flow. *Comput. Fluids* **23**, 251–278.

Leyrat-Maurin, A. & Barthés-Biesel, D. 1994 Motion of a deformable capsule through a hyperbolic constriction. *J. Fluid Mech.* **279**, 135–163.

Li, X., Charles, R. & Pozrikidis, C. 1996 Simple shear flow of suspensions of liquid drops. *J. Fluid Mech.* **320**, 395–416.

Loewenberg, M. & Hinch, E. J. 1996 Numerical simulation of a concentrated suspension in shear flow. *J. Fluid Mech.* **321**, 395–419.

Martinez, M. J. & Udell, K. S. 1990 Axisymmetric creeping motion of drops through circular tubes. *J. Fluid Mech.* **210**, 565–591.

Nakahashi, K. & Sharov, D. 1995 Direct surface triangular using the advancing front method. *Tech. Rep. AIAA*-95-1686-CP.

Olbricht, W. 1996 Pore-scale prototypes of multiphase flow in porous media. *Ann. Rev. Fluid Mech.* **28**, 187–213.

Olbricht, W. & Kung, D. 1992 The deformation and breakup of liquid drops in low Reynolds number flow through a capillary. *Phys. Fluids* A **4**, 1347–1354.

Pozrikidis, C. 1992 The buoyancy-driven motion of a train of viscous drops within a cylindrical tube. *J. Fluid Mech.* **237**, 627–648.

Pozrikidis, C. 1997 *Introduction to Theoretical and Computational Fluid Dynamics*. Oxford University Press.

Pozrikidis, C. 1998 *Numerical Computation in Science and Engineering*. Oxford University Press.

Queguiner, C. & Barthés-Biesel, D. 1997 Axisymmetric motion of capsules through cylindrical channels. *J. Fluid Mech.* **348**, 349–376.

Secomb, T. & Hsu, R. 1993 Non-axisymmetric motion of rigid closely fitting particles in fluid filled tubes. *J. Fluid Mech.* **257**, 403–420.

Shapira, M. & Haber, S. 1990 Low Reynolds number motion of a droplet in a shear flow including wall effects. *Intl J. Multiphase Flow* **16**, 305.

Skalak, R., Özkaya, N. & Skalak, T. 1989 Biofluid mechanics. *Ann. Rev. Fluid Mech.* **21**, 167–203.

Sugihara-Seki, M. 1996 Motion of an ellipsoid in tube flow of low Reynolds number. *J. Fluid Mech.* **324**, 287–308.

Sugihara-Seki, M. & Skalak, R. 1988 Numerical study of asymmetric flows of red blood cells in capillaries. *Microvasc. Res.* **36**, 64–76.

Sugihara-Seki, M. & Skalak, R. & Secomb, T. W. 1990 Two-dimensional analysis of two-file flow of red cells along capillaries. *Microvasc. Res.* **40**, 379–393.

Taylor, G. I. 1934 The formation of emulsions in definable fields of flow. *Proc. R. Soc. Lond.* **146**, 501–523.

Tsai, T. & Miksis, M. 1994 Dynamics of a drop in a constricted capillary tube. *J. Fluid Mech.* **274**, 197–217.

Tsai, T. & Miksis, M. 1997 The effect of surfactant on the dynamics of bubble snap-off. *J. Fluid Mech.* **337**, 381–410.

Zhou, H. & Pozrikidis, C. 1994 Pressure-driven flow of suspensions of liquid drops. *Phys. Fluids* **6**, 80–94.

Zinchenko, A. Z., Rother, M. A. & Davis, R. H. 1997 A novel boundary-integral algorithm for viscous interaction of deformable drops. *Phys. Fluids* **9**, 1493–1511.